Emergent Materials
https://doi.org/10.1007/s42247-025-01226-1

ORIGINAL ARTICLE

High-performance flexible temperature sensor based on heteroatom doped laser-reduced graphene oxide

Amin Nabawy[1] · **Mohammed Gamil**[2] · **Shaimaa A. Mohamed**[3,4,5] · **Amr Hessein**[1]

Received: 19 February 2025 / Accepted: 12 August 2025

Abstract

Wearable electronics and the Internet of Things (IoT) progression create a pressing desire to develop flexible sensors for healthcare monitoring and industrial applications. This study presents a new scalable and low-cost approach for fabricating high performance and flexible temperature sensors based on sulfur (S) and nitrogen (N) co-doped laser-reduced graphene oxide denoted as (LRSNGO) for wearable electronics. A handy visible laser engraver machine was fabricated for simultaneous co-doping, patterning, and photothermal reduction of graphene oxide (GO) films. SEM, XRD, and Raman spectroscopy results confirmed the effective photothermal reduction of GO and unveiled structural characteristics enhancements due to nitrogen and Sulfur co-doping. XPS analysis endorsed the efficient electron donative and defects curative integration of nitrogen and Sulfur heteroatoms into the graphitic lattice. The LRSNGO exhibited an electrical conductivity of 847.9 S/m significantly higher than the nitrogen-doped and the pristine LRGO. The LRSNGO also demonstrated the best thermal sensitivity, with a temperature coefficient of resistance (TCR) of −0.233%/ºC, which is ~117% higher than the pristine LRGO sensor. These results were associated with a fast response time of 3.5 s, excellent thermal stability, and outstanding mechanical stability and flexibility. LRSNGO sensor was tested for live monitoring of human body temperature demonstrated quick response and precision with an almost consistent body temperature reading. All characterization results are comprehensively discussed and interpreted throughout the study.

Highlights

- A scalable laser writing method is introduced for simultaneous doping, reduction, and maskless patterning of flexible graphene oxide thin films.
- The effects of heteroatom doping with nitrogen and co-doping with nitrogen and sulfur on the properties of laser-reduced graphene oxide films are thoroughly discussed.
- Remarkable enhancements in the structural and electrical properties of laser-reduced graphene oxide films upon the doping process were recorded.
- Flexible temperature sensors were fabricated and tested for wearable healthcare monitoring and IoT applications.
- The co-doped graphene-based temperature sensors showed outstanding temperature sensing performance compared to their counterparts, along with mechanical and cyclic stabilities.

Keywords Graphene oxide · Laser photothermal reduction · Graphene heteroatoms doping · Flexible temperature sensor · Wearable electronics

---

✉ Amin Nabawy
amin.abdelaal@feng.bu.edu.eg

[1] Department of Basic Science, Faculty of Engineering at Shoubra, Benha University, Cairo 11614, Egypt

[2] Department of Mechanical Engineering, Faculty of Engineering at Shoubra, Benha University, Cairo 11614, Egypt

[3] Nanotechnology and Nanoelectronics Engineering Program, University of Science and Technology, Zewail City of Science and Technology, October Gardens, 6Th of October, Giza 12578, Egypt

[4] Centre for Nanotechnology (CNT), Zewail City of Science, Technology and Innovation, Giza 12578, Egypt

[5] Nanotechnology and Nanoelectronics Engineering Program, Zewail City of Science, Technology and Innovation, Giza 12578, Egypt

1 Introduction

In daily life, human temperature is an essential parameter to measure in healthcare monitoring and industrial working fields [1]. Temperature sensing is playing a critical role in a wide range of modern technologies, including wearable health monitoring, smart cloths, and biomedical devices [2]. Flexible temperature sensors, which can be integrated into these applications, give precise readings while being mechanically flexible, allowing them to contour to the human body or other surfaces without losing functionality. Wearable health monitoring uses temperature sensors to check vital signs and detect health abnormalities such as fever or heat stress, ultimately improving patient care [3]. Similarly, smart cloths use temperature sensing to monitor body temperature in real time, hence promoting health and wellness [4]. Furthermore, in biological applications, flexible sensors are implanted or attached to monitor temperature changes, which is necessary for accurate diagnosis and therapy [5]. Overall, the integration of flexible temperature sensors into these applications not only improves performance but also expands the potential for innovative healthcare solutions [6]. Traditional rigid temperature sensors provide reliability and accuracy but often suffer from a lack of flexibility and scalability which limit their application in wearable electronics or IoT applications. By contrast, flexible temperature sensors offer many advantages, such as being soft, low cost, deformable, and able to take any customized designed patterns. These sensors usually consist of a heat-sensitive material layer on top of a substrate [7]. The sensitive layer must have a physical change with temperature, thermal stability against heating and cooling cycles, and low cost [8]. Current flexible temperature sensors have several limitations and challenges that affect their widespread use, performance, and reliability. Limitations such as fabricating sensors with promising performance parameters remain a significant challenge [9]. Also, employing difficult manufacturing procedures, toxic chemicals, and cost-effective materials creates a significant barrier to mass production [10]. Furthermore, production repeatability and reproducibility issues must be addressed to provide constant accuracy under varying situations [11]. Addressing these difficulties is critical to the development of flexible temperature sensor technologies.

Numerous materials were reported as resistive flexible temperature sensors including metals [12, 13], semiconductors and metal oxides [14, 15], conductive polymers [16, 17], carbon allotropes [18–20] and thin films of nanomaterials and nanocomposites [21, 22]. Among all studied materials, carbon allotropes such as graphene, carbon nanofibers (CNFs), and carbon nanotubes (CNTs) disclosed many advantages such as biocompatibility, flexibility, high thermal and electrical conductivities, rapid thermal response, and thermal stability. P. Sehrawat et al. investigated the heat sensing performance of the reduced graphene oxide (rGO) as a resistive sensor fabricated via spin coating of GO on an alumina substrate and reduced by thermal annealing. The authors reported a high TCR of ∼−0.801%/°C, in a high-temperature range of 30–300 °C, manifold higher than any commercial data or scientific findings [23]. Later, G. Liu et al. performed a series of experiments to compare the performance of the flexible temperature sensors fabricated from rGO, single-wall carbon nanotubes, and multiwall carbon nanotubes in the temperature range of 30 – 100 °C [2]. The experiments revealed that the best performance was recorded for the rGO-based sensor in terms of temperature sensitivity, performance linearity, and response time. Although the fabrication process was fairly complicated and lacked patterning capability, it established rGO as one of the strongest flexible temperature-sensing layer candidates for wearable electronics.

Graphene-based materials exhibited a negative temperature coefficient of resistance (NTCR). In pristine graphene, the conduction and valence bands are touched at the Dirac points and the density of states (DoS) near Fermi energy has a linear relationship with energy [24]. So, with the application of a temperature gradient, electrons thermalized from the valence band into the conduction band leading to an increase in the electrical conductivity with temperature. The situation is slightly different when it comes to the rGO. Not all oxygen groups are removed, and a part remains and the sp^2 network is partially restored [25]. Due to incomplete band structure, two conduction mechanisms were used to model resistance–temperature behavior in disordered materials like rGO. The variable range hopping mechanism (VRH) in a low-temperature regime and the nearest neighbor hopping mechanism (NNH) in a relatively higher-temperature regime [23]. In VRH, electron hops between localized states that are close in energy regardless of their spatial location in the lattice. Electrons can be boosted by electron–phonon scattering to overcome the difference between those localized states and complete the transition which is often described by Mott's law Eq. (1):

$$\sigma(T) = \sigma_o e^{-\left(\frac{T_o}{T}\right)^{1/(d+1)}} \tag{1}$$

where σ is the electrical conductivity, σ_o is a pre-factor, T_o is the characteristic temperature related to localization length and density of states, T is the system temperature, and d is the system dimensionality where $d=2$ for 2D systems and $d=3$ for 3D systems [23, 26]. In NNH on the other hand, electric conduction is primarily governed by thermal activation. At higher temperatures, electrons acquire sufficient energy, known as activation energy (E_a), which facilitates their hopping between the closest spatial atoms or the nearest available localized state regardless of their energy difference. This shortens the hopping mean-free path and improves electron mobility. The electric conductivity as a function of temperature in NNH is often described by the Arrhenius equation Eq. (2):

$$\sigma\left(T\right)=\sigma_{o}e^{-\frac{E_{a}}{K_{B}T}} \tag{2}$$

At room temperature and higher, both NNH and VRH mechanisms may coexist. As the temperature increases the hopping probability, and more conduction electrons are liberated too enhancing the electrical conductivity. This manifested as a decrease in the overall resistance of the rGO illustrating NTCR behavior. In addition to the commonly incomplete reduction of GO, structural defects evolved into graphene basal planes and at the edges [27]. For these reasons, lower TCR values are usually obtained for the rGO-based sensors [28, 29].

Heteroatom doping of rGO is a promising strategy usually adopted to improve the performance of rGO-based devices by tuning rGO electronic and structural qualities. Carbon neighbors in the periodic table such as boron [30], nitrogen [31], phosphorus [32], and sulfur [33] are commonly used to dope graphene. Heteroatoms such as nitrogen and sulfur have more electrons in the outermost shell and donate the excess electrons to the delocalized π-network to make n-type doping for graphene [34]. However, this depends in the first place on the locations where dopants are linked to the graphene lattice. Pyrrolic-N and thiophene functional groups are examples of n-type doping occurring by nitrogen and sulfur dopants, respectively. Graphitic-N and sulfoxides are other examples of N and S functionalities improving the rGO characteristics by curing the defective sites [35–37]. However, there is a scarcity of studies exploring the applications of doped graphene in flexible temperature sensors [38, 39]

In this regard, this study presents a simple yet effective approach for simultaneous co-doping, photothermal reduction, and patterning of GO thin films by laser writing for flexible temperature sensor applications. Thiourea, a single precursor for N and S dopants, was mixed with the exfoliated GO solution using ultrasonication. GO thin films on a flexible Polyethylene Terephthalate (PET) substrate were then fabricated by the drop-casting method. A visible diode laser-equipped engraving machine was built and used for the fast, scalable, and low-cost fabrication of flexible temperature sensors. Thanks to the ultrasonication and photothermal energies, S and N co-dopants were successfully integrated into the LRGO matrix as confirmed by XPS measurements. SEM, XRD, and Raman measurements analysis declared many structural variations of the LRSNGO in comparison to the pristine LRGO and the solely nitrogen-doped LRGO. The electrical and temperature sensing measurements showed remarkable enhancements in the LRSNGO sensor performance surpassing the other two devices. A high TCR of − 0.233%/°C was achieved for the LRSNGO sensor accompanied by a fast response time of 3.5 s. The results of all measurements are comprehensively discussed and interpreted in this study. The overall LRSNGO sensor performance enhancements were mainly attributed to combining the benefits and synergistic effects of co-doping with N and S in healing defective sites, donating excess free electrons, and promoting the mobility of free charge carriers.

2 Experimental work

2.1 Materials

Extra-pure graphite powder having a 5–20 µm grain size was purchased from Fisher Scientific. Urea granules [CH_4N_2O], and thiourea [CH_4N_2S] were obtained from Sigma Aldrich, Germany. All the other chemicals were reagent grade and used as received without any additional purification. Polyethylene Terephthalate (PET) Substrates with 100 µm thickness were locally sourced.

2.2 Preparation of doped GO films

Graphite oxide was prepared according to the modified Hummers' protocol [40–42] and explained in detail in the Supplementary information. The GO flexible thin films were prepared by drop-casting technique on a flexible commercial PET Substrate. First, the GO solution with 5 mg/ml concentration was prepared by dispersing graphite oxide in double distilled water using magnetic stirring which was followed by ultra-sonication bath for 1 h. For the doping of GO, 20 wt% of urea in the case of N-doping and 20 wt% thiourea in the case of SN-doping were added to the GO solution and Subjected to a mild ultra-sonication process for 2 h in an ice bath. Cooling was maintained to avoid the GO overheating which may cause partial reduction of the GO and affect the casting process. For comparison purpose, a plain GO solution was prepared following the same method but without any additives. All prepared GO solutions were centrifuged at 3000 rpm for 20 min to remove the non-exfoliated graphite oxide particles. For the casting process, the PET Substrates were pre-cleaned with ethanol and distilled water and dried at room temperature. 20 ml of the GO solution was uniformly drop-casted on a predefined 100 mm × 100 mm area with the help of an adhesive tape on the cleaned PET. The fabricated GO films were left to completely dry naturally at ambient conditions for at least two days before the laser reduction process.

2.3 Laser reduction and sensor fabrication

A custom-built CNC laser engraving machine equipped with a 450 nm wavelength diode laser with 10 Watts maximum power was employed for the laser reduction process of the prepared GO deposited on the flexible PET substrate (see the supplementary information Fig. S1). For the reduction process, the GO flexible films were located exactly at the laser's focus point. The laser machine parameters were manipulated until the lowest possible sheet resistance was achieved without any visual damage or cracks observed in the samples. The optimized laser reduction conditions were set to an engraving speed of 600 mm/min, 5% of laser power, and 20 lines per mm resolution for all the fabricated samples. A summary of the fabrication workflow of the laser reduction process is schematically shown in Fig. 1.

2.4 Material characterization

The surface morphologies of the prepared samples were studied using a scanning electron microscope "SEM" (ThermoFisher (USA) Quattro S Felid Emission Gun, Environmental SEM "FEG ESEM"). The structural analysis of the prepared samples was studied using Raman spectroscopy and x-ray diffraction (XRD). Raman scattering spectra were collected using a Confocal Raman Microscope (WiTec, 300R alpha). The measurements were performed with a 532 nm laser wavelength, 2 mW laser power, Accumulation time of 10 s, and overall integration time of 10 s. The XRD patterns for the prepared samples were recorded using a Rigaku Miniflex600 Benchtop diffractometer operating with a Cu target as Kα x-ray radiation source of wavelength (λ = 1.5418 A°). X-ray photoelectron spectroscopy (XPS) spectra was measured using (SPECS- Surface nano analysis GmbH, Germany with x-ray beam source Al 400w, 15 kV). Finally, we employed a four-point probe instrument (Ossila, UK) for the sheet resistance measurements.

2.5 Temperature sensor measurements

The performance of the fabricated temperature sensor samples was evaluated in terms of temperature sensitivity, linearity, stability, response time, and recovery time. Sensor's sensitivity was measured by a custom-built setup. The sensor under test was fixed on the hot surface of a commercial Peltier element (TEC1-12706) that is connected to a variable DC power supply. The sensors' resistances were recorded by means of Keithley 2400 using a Paios two-point flexible probe station. A K type thermocouple with a digital multimeter (UNI-T UT39C+) was attached to the sensor surface to measure its actual temperature. The sensors' flexibility and mechanical stability were examined by a custom-built mechanisms (*see* supplementary information Fig. S2).

3 Results and discussion

The oxidation process of graphite create functional groups such as hydroxyl (-OH), carbonyl (C=O), and carboxyl (-COOH) within the graphite structure which increased

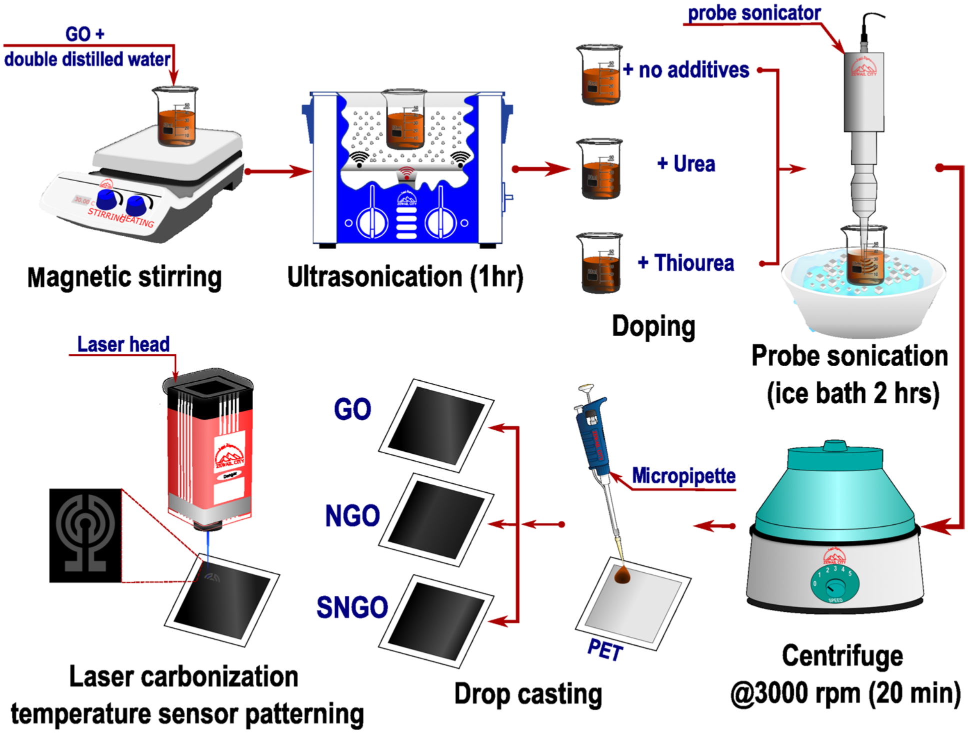

Fig. 1 Sample preparation procedures, laser carbonization, and temperature sensor patterning

the graphitic interlayer distances and facilitate the liquid phase exfoliation process Fig. 2a [43, 44]. That which was confirmed by the XRD measurements acquired for the graphite before and after the oxidation process, and also by the FTIR and XPS analysis of graphite oxide, as shown in Fig. S3. Herein, a proposed approach for simultaneous doping, photothermal reduction, and maskless patterning process with visible laser light for GO flexible films is introduced. The approach mechanism starts with a simple chemical mixing followed by an ultrasonic-assisted process which can be explained as follows: First, urea or thiourea granules were added to the GO solution. The mixture was subjected to mild ultrasonication for the GO exfoliation purposes. During the ultrasonication also, the urea is broken down into nitrogen-containing moieties such as ammonia whereas thiourea on the other hand is dissociated to sulfur and nitrogen moieties such as ammonia and thiocyanate [45]. These moieties are attached to the edges and basal planes of the exfoliated GO sheets with the assistance of the aforementioned oxygen functional groups and also the defective sites on the graphitic sheets evolved during the oxidation process, Fig. 2b After that, when the GO films are illuminated with visible laser pulses, the GO absorbs the photon energy, and heat is generated. When the laser intensity is beyond a specific threshold, an enormous amount of heat is generated (>1000–2500 °C) which is enough to break C−O and C=O bonds and remove the oxygen functionality from the GO sheets [46]. An expansion of the LRGO film thickness is visually observed which is mainly attributed to the fast liberation of gases from the films during the photothermal reduction process. Besides the photothermal GO reduction, it is supposed also that the heat generated from the absorption of the laser power is used to integrate the nitrogen and sulfur heteroatoms into the LRGO sheets, Fig. 2c-d. Hence, a variation in the structural and electrical properties of the LRGO films is supposed to be noticed due to nitrogen doping and sulfur-nitrogen co-doping.

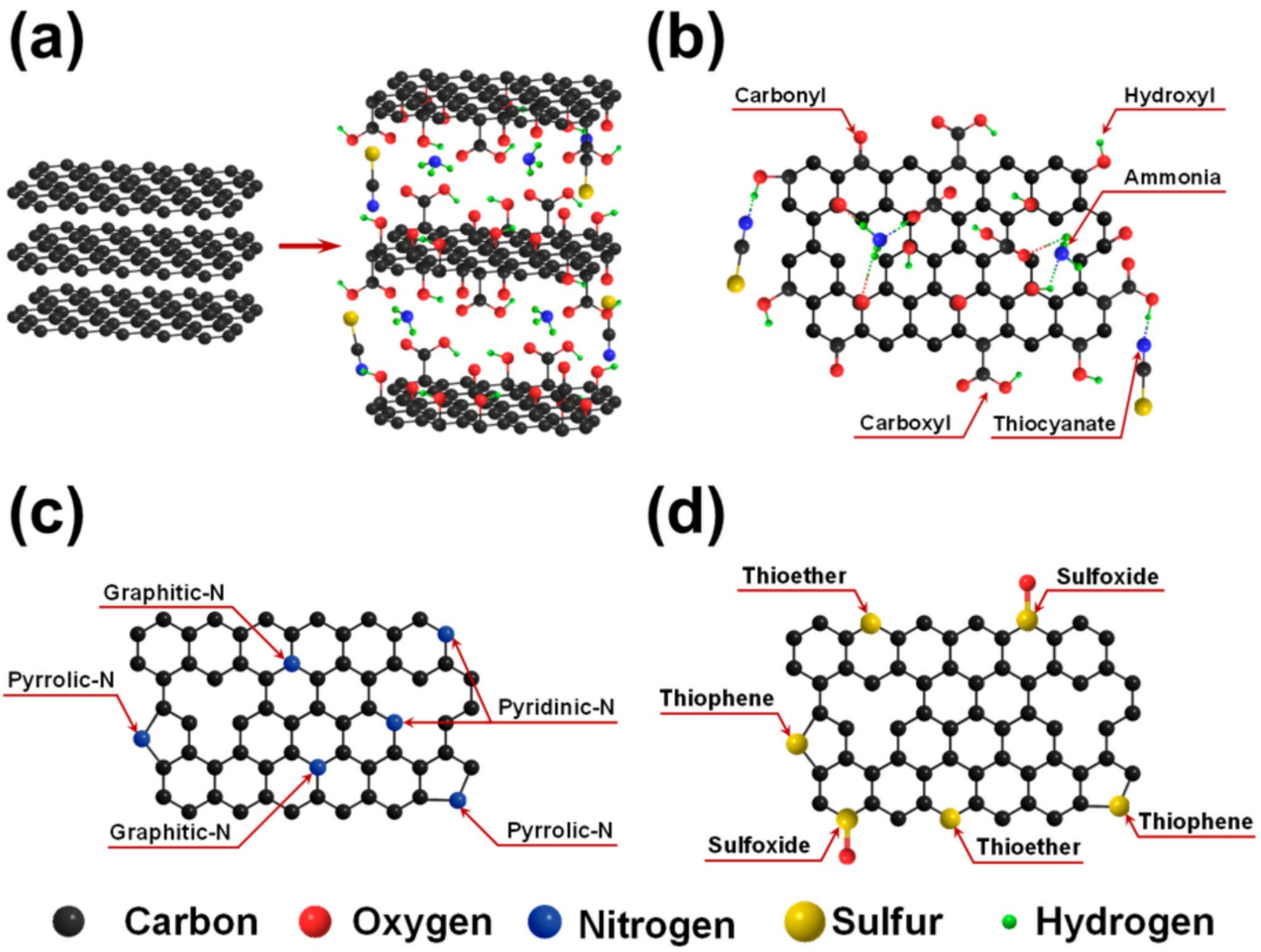

Fig. 2 (**a**) graphite oxidization by Hummer's method (**b**) oxygen functional groups, ammonia, and thiocyanate position in GO structure (**c**) nitrogen atom positions in LRNGO structure (**d**) sulfur atom positions in LRSNGO structure

3.1 Structural analysis

SEM microscopy was used to evaluate the morphology changes in the flexible GO before and after the laser treatment. Figure 3a shows a typical SEM micrograph of the as-casted GO film that is covered by wrinkles arising from the oxygen functional groups linked to the graphitic sheets of the GO and preventing it from restacking [47]. The existence of such a large number of wrinkles on the surface indicates the excellent exfoliation process of the GO by mild ultrasonication in water. The absence of any surface cracks or pores in the surface is an indication for the high-quality GO films on the flexible PET substrate using the drop-casting method. Upon the laser photothermal reduction process, the SEM images revealed several variations in the surface morphology of the GO films after the laser photothermal reduction process was conducted. The micrograph of the pristine LRGO in Fig. 3b shows clearly the traces of the laser pulses and the disappearance of the surface wrinkles confirming the successful laser reduction process. The image also reveals the porosity of the LRGO film surface morphology that consists of overlapping graphene nanoflakes comprising several unordered graphene sheets stacking together. This was accompanied by the evolution of some micropores resulting from the fast-gaseous release by the laser photothermal reduction process. All laser-reduced films (LRGO, LRNGO, and LRSNGO) showed similar surface morphologies. Similar observations were previously reported for GO films photothermal reduced by different laser wavelengths [48, 49].

A noticeable volume increase at the GO and LRGO interface after the laser reduction was observed in the cross-section micrograph of the LRGO in Fig. 3c. The volume expansion demonstrates the increased interlayer spacing between the graphene sheets due to the gases liberation during the laser reduction process. The average film thicknesses of the three fabricated films were estimated from the cross-section micrographs Fig. 3c–e. The LRGO average thickness was ~ 25.7µm which increased in the case of LRNGO to ~ 33.15 µm, whereas the LRSNGO's average thickness was only ~ 26.2 µm. The largest thickness of the LRNGO could be attributed to the ability of the nitrogen atoms incorporated into the graphene hexagonal lattice at different configurations creating more lattice distortion that led to an increase in the interlayer spacing [50]. Meanwhile, the smaller LRSNGO's average thickness may be due to the nature of sulfur doping which occurs mostly at graphene sheets edges and defects sites without distorting the carbon hexagonal lattice. This could be strongly confirmed by the high magnified cross-section micrographs in the insets

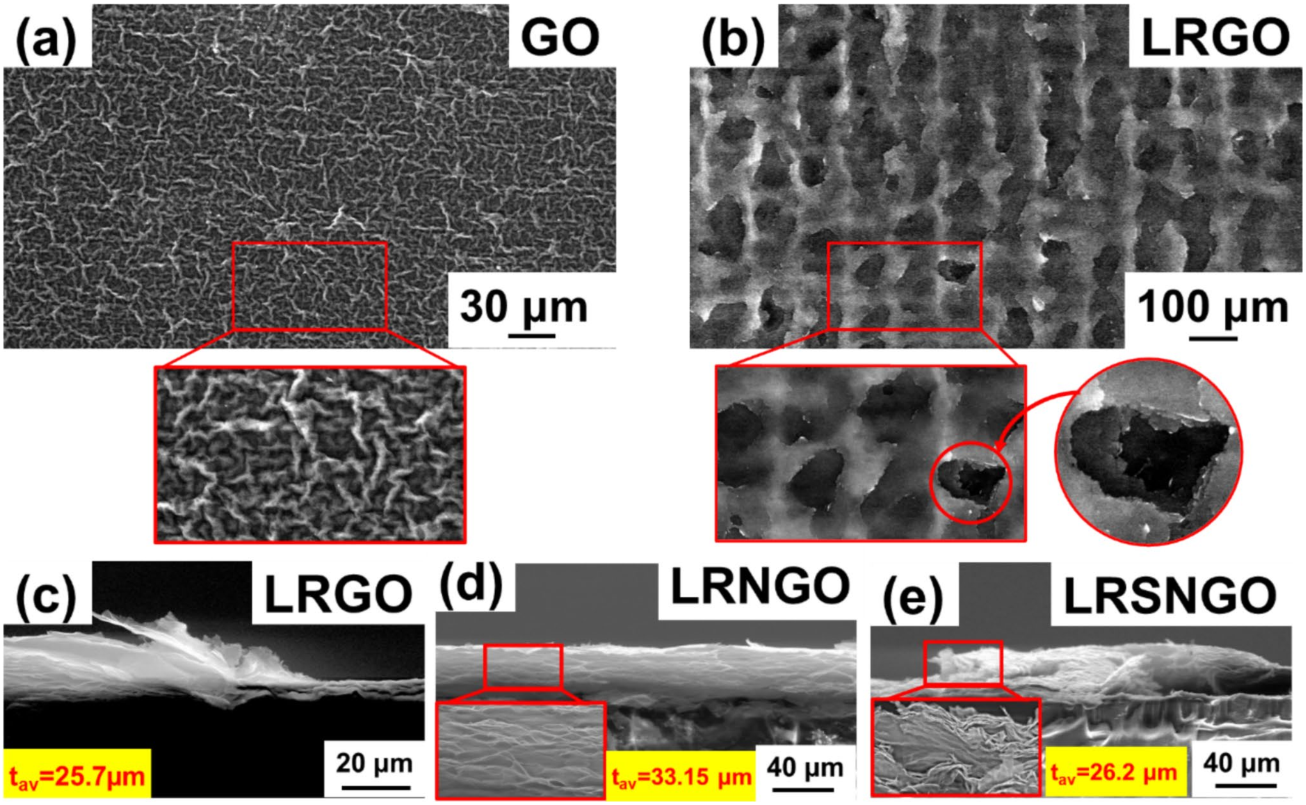

Fig. 3 SEM micrographs of (**a**) GO surface before reduction (**b**) LRGO surface with pores (**c**) LRGO cross section (**d**) LRNGO cross section (**e**) LRSNGO cross section

of Fig. 3d-e that show the LRSNGO is composed of more densely packed graphene sheets than the LNRGO which could be beneficial for better electric conductivity of the co-doped films.

Figure 4a shows the XRD patterns collected for the LRGO, LRNGO, and LRSNGO films and compared with that of the GO. The XRD pattern of the GO shows a graphite oxide characteristic peak at 2θ = 10.08° indexed to the (001) reflection plane with an interplanar spacing of d≈0.879 nm [51]. This peak has completely disappeared in the other three laser-reduced films. Instead, a sharp characteristic peak centered around 2θ ≈ 25.8° and indexed to the interplanar spacing of d≈0.345 nm for the graphitic (002) planes. This demonstrates that the laser reduction removes oxygen functional groups. The slight downshift obtained in the (002) XRD peak for the laser-reduced samples from the 2θ = 26.4° of graphite is attributed to the expanded morphology of the samples and also to the lattice imperfections [51]. The measured FWHM of the (002) peak for the LRGO, LRNGO, and LRSNGO are 0.6387°, 1.2622°, and 1.2277° respectively. The broader the peak, the more exfoliated the graphene sheets [52]. Hence the lower FWHM of the LRSNGO compared to that of the LRNGO agrees well with the previous SEM findings that the sole N doping produces more expanded graphene sheets than the SN co-doping.

Nondestructive Raman spectroscopy was employed to evaluate the laser reduction efficiency, sample quality, and structural defect density of the GO films. Figure 4b and Fig. S4 show the recorded Raman spectra for the three fabricated films before and after the laser process. The three characteristic graphitic carbon Raman peaks, D (~1345 cm^{-1}), G (~1575cm^{1}), and 2D (~2695cm^{-1}) are clearly seen in the measured spectra [53–55]. However, a sharp decrease in the defective peak intensity (I_D) alongside a remarkable increase in the graphitic peak intensity (I_G) in all three samples was achieved after the photothermal reduction process. This unequivocally confirms the successful photoreduction process of the GO films by the visible laser. Table (S1) summarizes the parameters estimated from the Raman data analysis. The lowest I_D/I_G ratio was calculated for the LRSNGO which emphasizes the role of sulfur and nitrogen atoms in healing the structural defects in the graphene sheets during the deoxygenation process [54]. These observations also ascertain the role of sulfur and nitrogen heteroatoms

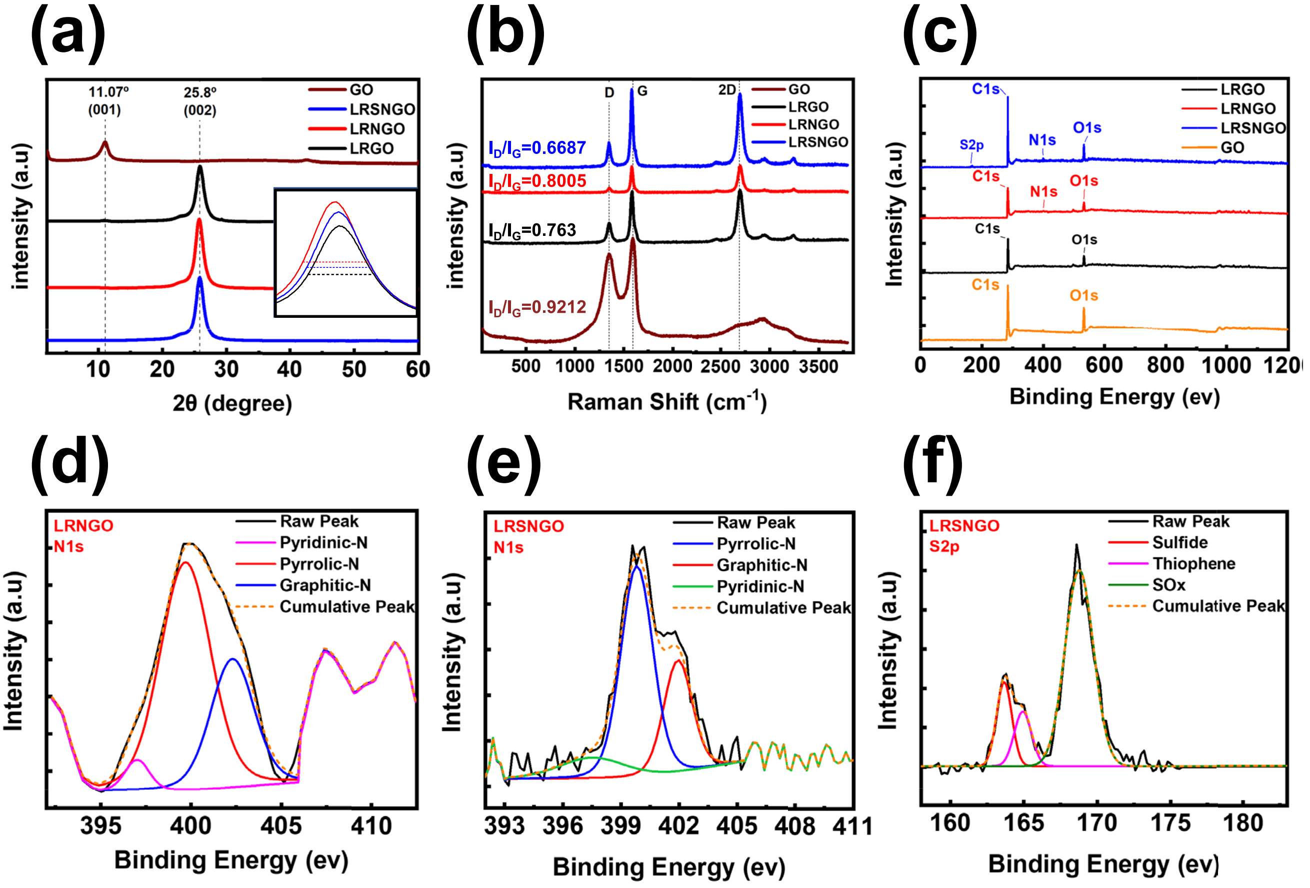

Fig. 4 Material characterization (**a**) XRD pattern for GO and laser-reduced samples (**b**) Raman Spectrum for all reduced samples stacked compared with GO (**c**) XPS survey spectra for LRGO, LRNGO, LRSNGO, and GO (**d**) deconvolution of N1s peak of LRNGO (**e**) deconvolution of N1s peak of LRSNGO (**f**) deconvolution of S2p peak of LRSNGO

doping in enhancing the graphitization degree of the GO by the photothermal reduction process. Nonetheless, both LRNGO and LRSNGO samples showed a decrease in the G-peak FWHM. Graphene doping was reported to shift the Fermi level away from the Dirac point decreasing the carrier recombination probability which leads to Raman G-peak sharpening [53]. Thus, the sharpness obtained in the G-peak and the slight redshift in the 2D-peak of the LRNGO and LRSNGO samples suggest successful doping during the laser processing. Also, the I_{2D}/I_G ratios are around unity for the three laser-reduced samples corresponding to the bilayer and few-layer graphene sheets reflecting the effective deoxygenation and exfoliation process of the graphene sheets by the visible laser [56]. Furthermore, the ratio $\mathrm{I_D/I_G}$ was used to estimate the average distance between defects (L_D), defect density per cm^2 (η_D), and domain size ($L_{sp}{}^2$) for the LRGO, LRNGO, and LRSNGO films using Eq. (3) – (5) and the obtained results are summarized in Table 1:

$$L^2{}_D\left(nm^2\right) = \left(2.4\times 10^{-9}\right)\lambda_L{}^4\left(\frac{I_D}{I_G}\right)^{-1} \tag{3}$$

$$\eta_D = \frac{2.4\times 10^{22}}{\lambda_L{}^4}\left(\frac{I_D}{I_G}\right) \tag{4}$$

$$L_{sp^2} = \left(2.4\times 10^{-10}\right)\lambda_L{}^4\left(\frac{I_D}{I_G}\right)^{-1} \tag{5}$$

where λ_L=532 nm is the excitation [57, 58]. Table 1 illustrates that nitrogen atom doping in graphene lattice increased the number of defects. As a result, the average distance between successive defects (L_D) and sp^2 domain size ($L_{sp}{}^2$) of the LRNGO decreased compared to that of LRGO. Additionally, the defect density (η_D) of the LRNGO increased compared to that of LRGO, indicating that the LRNGO was more disordered and had a smaller sp^2 domain size. the LRSNGO demonstrated the lowest defect density and the larger average distance between the successive defects. In addition, the LRSNGO exhibited the largest sp^2 domain size. This exposes the synergistic role of SN co-doping and laser reduction in producing high-quality graphene sheets desired for good electrical conductivity and high temperature sensing performance.

To determine the accurate elemental composition of the fabricated samples, XPS measurements were performed. Figure 4c shows the survey spectra of GO, LRGO, LRNGO, and LRSNGO respectively. The C1s and O1s peaks appeared at 284.5 eV and 532.3 eV, respectively, in all samples [59, 60]. Whereas N1s peak appeared at 400 eV in the LRNGO and the LRSNGO samples, and an additional S2p peak appeared at 163.8 eV in the LRSNGO sample [48, 55, 61, 62]. The estimated elemental compositions of the samples from the XPS measurements are tabulated in Table 2. The estimated results show that laser reduction reduces the oxygen content in the films, which directly increases the C/O ratio of all samples**.** The presence of oxygen in laser-reduced samples implies the partial reduction of the GO films. Whilst the existence of N1s peak in the LRNGO spectrum and the N1s and S2p peaks in the LRSNGO spectrum confirm the successful integration of the heteroatoms into the graphene framework. The relatively weak peaks for the N and S are because of their significantly lower concentrations compared to carbon and oxygen.

N1s and S2p peaks deconvolution study used to explore how the heteroatoms were linked to the graphene framework. Figure 4d gives the deconvoluted N1s peak of the LRNGO. The deconvolution manifested that three types of nitrogen functional groups, namely pyridinic-N [(397 eV) – (4.26%)], pyrrolic-N [(399.69 eV) – (64.62%)], and graphitic-N [(402.2 eV)-(31.12%)] were formed [55, 63]. Both pyrrolic-N and graphitic-N are working as electron donors for the delocalized π network of graphene [64]. Hence, a reduction in the sheet resistance of the LRNGO is expected to be observed. Also, the N1s deconvolution of the LRSNGO in Fig. 4e declared high contributions for the pyrrolic-N and graphitic-N functionality. Figure 4f is the deconvoluted of the LRNGO S2p peak which declared the formation of three types of sulfur functional groups C-S-C [(163.7 eV)—(16.5%)], thiophene [(164.9 eV)—(12.1%)], and -SOx [(168.8) – (71.4%)]. Thiophene functionality donates two delocalized electrons to the π network. The other two Sulfur forms modulate the electronic band structure via the creation of localized states near the Fermi level and induce spatial distortion preventing graphene sheets from order restacking [65]. For these reasons, the co-doped LRSNGO is highly suggested to surpass the performance of the other two samples.

Table 1 Estimated parameters from Raman scattering measurements: average distance between defects (L_D), defect density per cm^2 (η_D), and sp^2 domain size ($L_{SP}{}^2$) Raman results

Sample	L_D (nm)	η_D (cm^{-2})	$L_{SP}{}^2$ (nm)	I_D/I_G	I_{2D}/I_G
LRGO	15.873	2.286×10^{11}	25.197	0.763	1.0101
LRNGO	15.497	2.399×10^{11}	24.015	0.8005	1.0115
LRSNGO	16.956	2.003×10^{11}	28.752	0.6687	0.974

Table 2 Elemental composition of GO, LRGO, LRNGO, and LRSNGO determined from the XPS analysis

	C at %	O at %	N at %	S at %
GO	65.7	34.3	-	-
LRGO	73.83	26.17	-	-
LRNGO	73.61	24.02	2.37	-
LRSNGO	68.86	26.84	3	1.3

3.2 Electrical measurements

The laser parameters were optimized to ensure the best reduction efficiency and electrical performance for the fabricated graphene-based temperature sensors. A laser speed of 600 mm/min and Line spacing of 0.05 mm had been found the best suited for the GO/PET samples. The laser reduction power was varied from 4% to 6.5% of the maximum power (10 Watts) by a step of 0.5%. Figure 5a shows the variation of the sheet resistance measured for 10 mm × 10 mm films of the LRGO, LRNGO, and LRSNGO, and the laser power. All reduced samples showed a sharp reduction in sheet resistance with increasing the laser power from 4% to 5.5% implying better GO reduction by increasing the absorbed photothermal power. Further increases in laser power beyond 6.5% did not Substantially lower the sheet resistance of the samples. It is clear that both the doped LRNGO and LRSNGO had lower sheet resistance than the LRGO at all tested laser powers. Moreover, the LRSNGO achieved the lowest sheet resistance at all power values. This emphasizes the role of laser photoreduction in conjunction with doping in improving the electric conductivity of the GO films. This also agrees with our findings that S and N co-doping is more efficient for healing the graphene lattice structural defects and donating more charge carriers than N doping alone. Herein, 5% laser power was Chosen as the optimum value due to its better mechanical stability. Beyond 5% some destroying visually seen on the laser-reduced films, see supplementary Fig. S5.

The bulk conductivity of the laser-reduced films was calculated from Eq. (6):

$$\sigma = \frac{1}{R_s t} \tag{6}$$

where σ (S/m) is the bulk conductivity, Rs (Ω/sq) is the sheet resistance, and t (m) is the average thickness in estimated from the SEM cross-section measurements [66]. Figure 5b shows a comparison between the bulk electrical conductivity (σ) of the three prepared films. The highest electrical conductivity of 847.9 S/m was calculated for the LRSNGO film given that it recorded the lowest sheet resistance of ~ 45 Ω/sq. The LRNGO and LRGO attained nearly similar electrical conductivity although the sheet resistance of the LRNGO was lower. This is because the LRNGO attained a more expanded cross-section among the three films as discussed earlier.

3.3 Temperature sensor performance characterization

Figure 6a shows a photograph of the custom-built temperature sensor characterization setup. The sensor under investigation was fixed to the hot side of the Peltier element and it's temperature was adjusted by varying the applied DC voltage. A two-point probe station connected to Keithley 2400 measures the sensor's resistance as a function of temperature. A multimeter equipped with a thermocouple was used to read the sensor's actual temperature. It is worth mentioning that the whole system was covered during the measurement to prevent heat loss and to provide stable reading.

Among the different patterns reported in the literature for flexible temperature sensors, the heater pattern presented in Fig. S6 was employed in this study. Compared to square and serpentine widely reported, for example, [67, 68] the heater pattern exhibits longer electric conduction path and larger thermal mass. The fabricated and tested resistive temperature sensors were the LRGO (3.71 kΩ), LRNGO (2.58 kΩ), and LRSNGO (1.79 kΩ). The lower overall

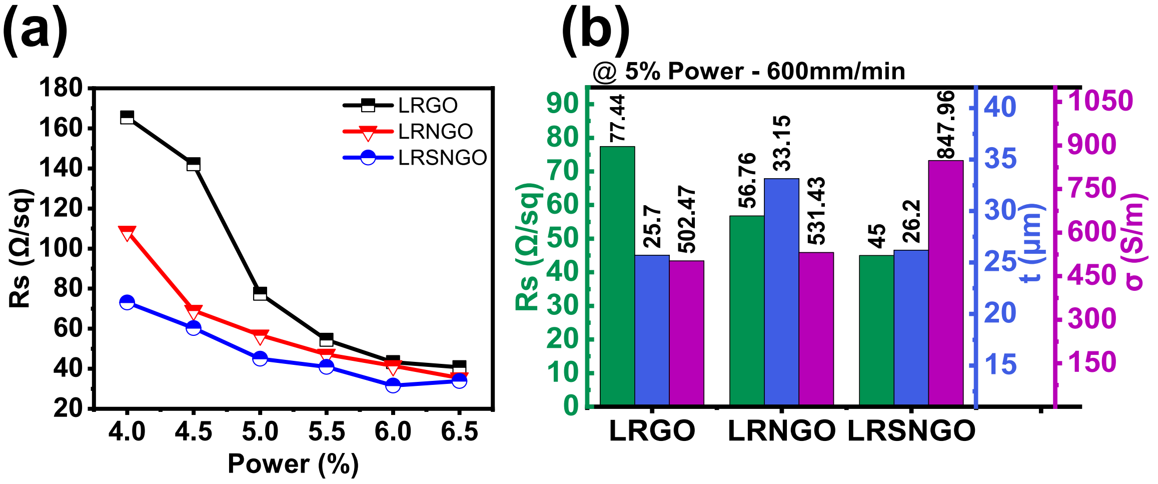

Fig. 5 (**a**) sheet resistance variation with laser power for LRGO, LRNGO, and LRSNGO (**b**) Estimated values of the sheet resistance (R_s), average thickness (t_{av}), and electrical conductivity (σ) at 5% laser power for LRGO, LRNGO, and LRSNGO films

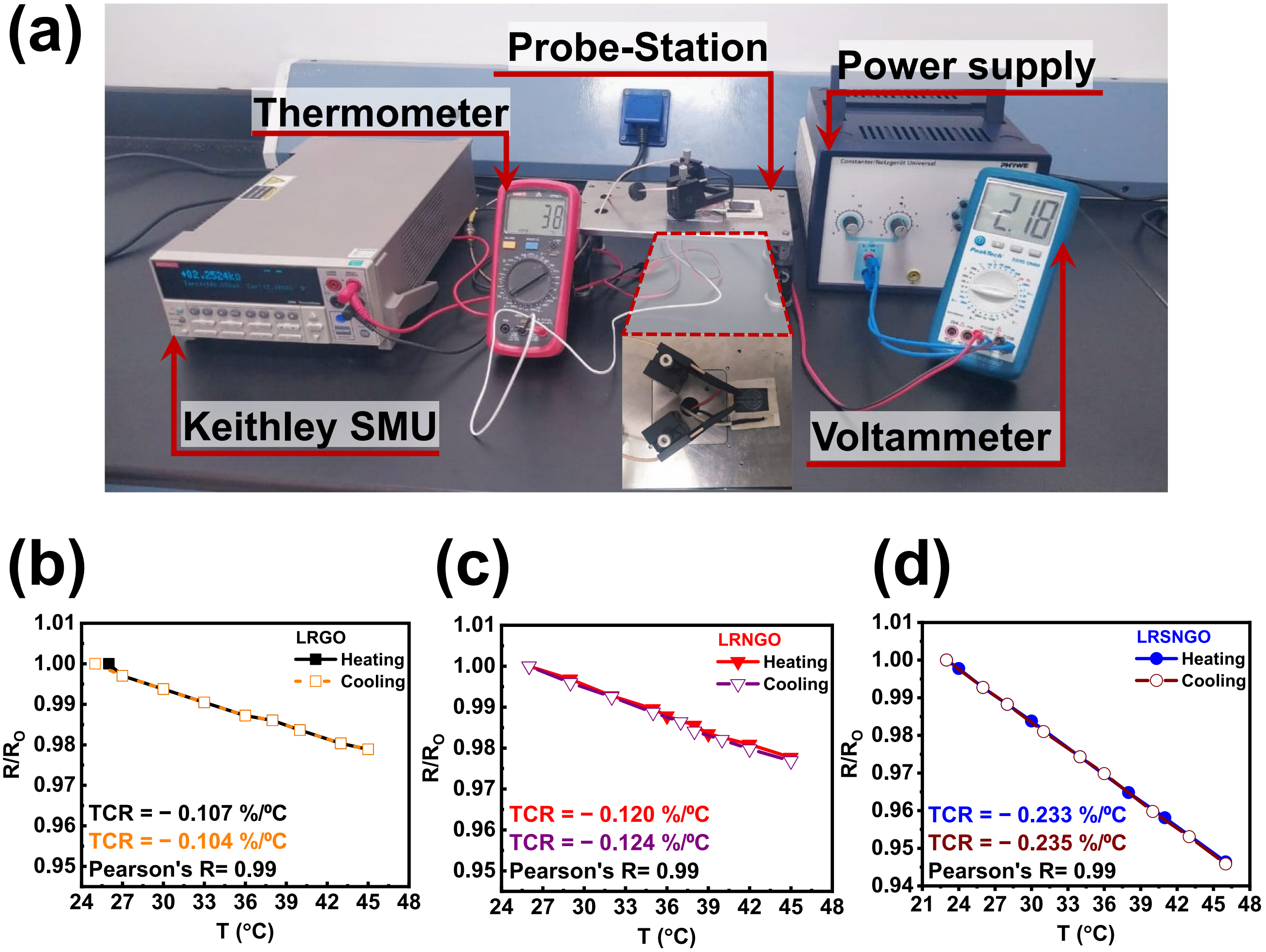

Fig. 6 **a** Photograph for the custom-built temperature sensor characterization setup, (**b**) R/R$_0$% versus temperature indicating resistance temperature coefficient (TCR) for LRGO, (**c**) LRNGO, and (**d**) LRSNGO

LRSNGO sensor resistance is due to its higher bulk electrical conductivity. Figure 6b-d gives the relationship between (R/R$_0$) % and T measured in the temperature range (25–45 ºC) for the fabricated sensors during heating and cooling sweeping directions. The figure disclosed that all the sensors experienced resistance decreases as the temperature increased indicating their NTCR nature. All sensors displayed negligible hysteresis between the heating and cooling measured data. Also, the measured data are well-fitted straight lines as indicated with Pearson's coefficient (*R*) close to unity. These results indicate the perfect temperature sensing mechanism of all the fabricated LRGO films and also the higher accuracy of the measurements. Interestingly, at the end of the heating and cooling tests, all fabricated sensors successfully restored their initial resistances reflecting good reversibility.

The temperature Sensor's sensitivity is determined by the resistance temperature coefficient (TCR) which is calculated from Eq. (7) [69]:

$$TCR = \frac{\Delta R / R_o}{\Delta T} \tag{7}$$

where R_o is the sensor's resistance at room temperature and ΔR is the change in sensor resistance at temperature difference ΔT from room temperature. The TCR of the pristine LRGO sensor was calculated to be − 0.101%/°C, The LRNGO sensor showed a 19.4% improvement in the TCR and recorded − 0.1206%/°C because of its relatively lower resistance. The superior temperature sensitivity was exhibited by the LRSNGO sensor that achieved a TCR of − 0.233%/°C, which is ~ 117% enhancement to the sensitivity of the pristine LRGO sensor. The TCR of the pristine LRGO sensor closely matches previously reported values for graphene-based sensors as seen in the performance comparison Table 3. This demonstrates the high caliber of the custom-built visible laser machine for the GO reduction, and also the temperature sensitivity characterization system. Electrical resistance is inversely proportional to electrical conductivity, so Arrhenius equation Eq. (2) can be modified to:

$$R(T) = R_o e^{\frac{-E_a}{K_B T}} \tag{7}$$

and taking the natural logarithm, we get Eq. (8):

$$\ln\left(\frac{R_o}{R}\right) = \frac{E_a}{K_B T} \tag{8}$$

By drawing a relation between $\ln\left(\frac{R_o}{R}\right)$ and $1/T$ it should give a linear relationship with slope equal to E_a/K_B. Figure 7a shows the plot between ln (R) and ($1/T$) for the three sensors which are best fitted to linear relationships and implying NNH is the dominate conduction mechanism in all samples. The estimated activation energy of the LRSNGO (19.4 meV), LRNGO (10.12 meV), and LRGO (8.41 meV) are all below the 25.9 meV of the room temperature activation energy. The higher activation energy of the LRSNGO may be associated with the relatively larger average sp^2 domain size (~28.7519 nm) formed by the SN-Co-doping than the other two samples as found earlier from Raman data analysis [70, 71].

As discussed earlier, NNH transport conduction features electron tunneling and hopping between the neighboring sp^2 domains mechanism in rGO. Three major parameters, namely, the electronic properties, the structural defects, and the thermal electron transport, are thus controlling the temperature sensitivity of the graphene-based sensors [72]. To more elaborate, doped graphene with heteroatoms such as N and S exhibits n-type semiconductor conductivity. According to the XPS findings, higher concentrations of the electron donator Pyrrolic-N (59.85%) and graphitic-N (28.34%) were formed in the LRSNGO (3% N) than Pyrrolic-N (64.62%) and graphitic-N (31.12%) in the LRNGO (2.37% N) besides the S-based thiophene electron donator (12.1%). The higher the free electrons are, the higher the electric conductivity. Also, the S and N co-doping contribute to the healing of the laser-reduced graphene structural defects which lower electron scattering. Thus, raising the temperature of the LRSNGO—enriched with more free electrons than the other two sensors—increased the electron tunneling and hopping mobility rates, leading to the superior temperature sensitivity that was achieved. Table 3 conveys the superiority of the LRSNGO sensors such that the TCR of −0.233%/°C, is far overcoming most of the recently reported values for graphene-based flexible temperature sensors fabricated with laser processing or other fabrication techniques.

The sensor response time is an essential parameter used to assess the feasibility of the sensor for practical applications. So, a temperature responsivity measurement experiment for the fabricated sensors was designed and executed to estimate their response time. Two wires were connected to the sensor under test using silver paste, those used to make the sensor connection with the Keithley – 2400 meter. To suddenly increase the sensor's temperature, hot water was quickly poured into the stainless-steel cup that was attached to it, as seen in Fig. S7 the change of the sensor's resistance against time was recorded. The flexible LRSNGO temperature sensors realized an immediate change in resistance upon the sudden heating, see supplementary video VSI1. The response time of the sensor is defined as the required time till sample resistance reached 63.2% of the final steady-state value [79]. Figure 7b shows the response time measurements for the LRGO, LRNGO, and the LRSNGO

Table 3 Performance comparison between the LRSNGO sensor from this work and the most recent published graphene-based temperature sensors

Sensing material	Substrate	Temperature range (°C)	TCR (%/°C)	Response time (s)	recovery time (s)	Ref
LRGO	PET	30–50	−0.101	≈ 3.5	-	(this work)
LRNGO	PET	30–50	−0.1206	≈ 3.5	-	(this work)
LRSNGO	PET	30–50	−0.233	≈ 3.5	7.3	(this work)
r-GO	PI	30–40	−0.28	0.6	0.6	[73]
r-GO	Paper	30–100	−2.77	5.5	5.1	[74]
r-GO	PET	30–100	−0.37	0.196—0.274	9.7	[69]
LIG	PI	25–60	−0.068	3	-	[67]
LCBFs	PAN (CNFs)	25–60	−0.087/ −0.114/ −0.127	20	-	
graphene nanoplatelets	alumina	10–100	−0.0052	125	-	[75]
r-GO		10–100	−0.00486	121	-	
r-GO		30–100	−0.008	1.2	-	[2]
MWCNTs	PET	30–100	−0.0063	-	-	
Laser-induced graphene (LIG)	PI	−10–60	−0.0014	1 ≈ 20	-	[76]
LIG	paper	30–45	−0.15	-	-	[77]
LIG	PI	30–100	−0.05	2	3.9	[78]

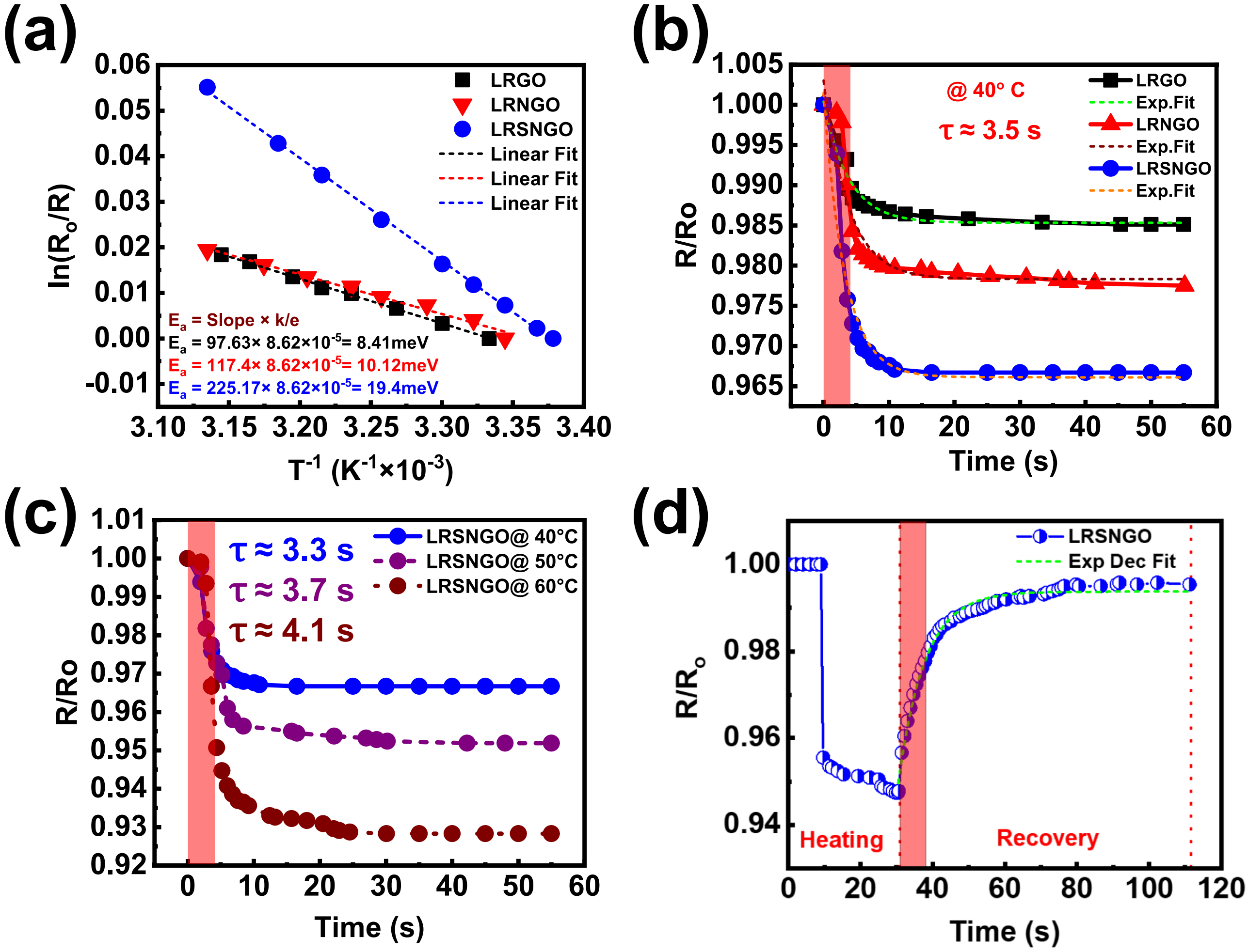

Fig. 7 (**a**) Arrhenius equation validation of LRGO, LRNGO, and LRSNGO, (**b**) normalized graphs of response time and exponential fit of LRGO, LRNGO, and LRSNGO at 40 °C (**c**) response time of LRSNGO at 40 °C, 50 °C, and 60 °C (**d**) Recovery time of LRSNGO at 40 °C

sensors measured at temperature of 40 °C. An exponential fitting for the recorded data was performed according to the following Eq. (9) [69]:

$$\frac{R}{R_o}(t) = \left(\frac{R}{R_o}\right)_o + A_1\exp\left(\frac{-(t-t_o)}{\tau}\right) \rightarrow \qquad (9)$$

where $\frac{R}{R_o}(t)$ is the normalized resistance as a function of time, $\left(\frac{R}{R_o}\right)_o$ baseline value which the function approach it at infinity, A_1 initial amplitude, t is time as the independent variable, t_o is the time offset at which the decay begins, and τ is the time constant represent response time or recovery time. The fitted response time was estimated $\tau \approx 3.5$ s for the three sensors, which is comparable with literature tabulated in Table 3. The response time is to some extent dependent on the material response as well as on those of the PET Substrate and the stainless steel. However, it is worth mentioning that the LRSNGO consumed 3.5 s of response time to make a larger ΔR than the other two devices. Figure 7c shows a sharp decrease in the response time of the LRSNGO sensor as the applied temperature difference is increased. This is mainly attributed to the enhanced electron speed braking by the electron–phonon scattering that increased as the temperature increased.

Recovery time is the time in which the sensor's resistance returns to 63.2% of its initial value after a sudden removal from a high-temperature region and permitting it to cool naturally. The experiment was performed following the procedure reported in Ref. [69] by heating the freely hanging LRSNGO sensor to a temperature of 40 °C with a hot air gun, see supplementary information Fig. S8. Once reached a steady-state condition at the target temperature, the heating source was removed, and the sensor resistance was acquired versus time, see supplementary video VSI1. The acquired data in Fig. 7d was exponentially fitted using Eq. (9) and a reasonable recovery time τ~7.3 s was estimated for the LRSNGO temperature sensor. Our estimated recovery time was comparable with the reported in Table 3, The recovery time is somewhat influenced by the heat that flows through the substrate; in other words, the substrate's thermal conductivity influences the recovery time; the higher the thermal conductivity, the faster the heat is released from the sensor. Our substrate, PET, has poor thermal conductivity, which had an undesirable effect on recovery time.

The thermal stability of the LRSNGO sensor was tested by repeating the temperature sensitivity measurement five times within the same range of temperature. As seen obviously in Fig. 8a, the LRSNGO sensor was able to deliver nearly similar temperature sensitivity output during the five testing cycles. This proves its good thermal stability and suitability for transient wearable applications. The long-term stability test as well was performed on the LRSNGO sensor. Figure 8b compares the temperature sensitivity between a fresh LRSNGO sensor and that of an LRSNGO stored under normal ambient conditions for five months. A negligible change in performance between the two devices is noticed. The TCR of the aged device is −0.233%/°C nearly identical to that of the fresh device (−0.233%/°C), confirming the excellent shelve storing stability attributed in the first place to the hydrophobicity and chemical stability of the LRSNGO. To validate sensor fabricating repeatability, four LRSNGO samples were fabricated and their sensitivity evaluated under precisely the same conditions. Figure 8c displays their TCR values, which displayed close performance with 0.0176 standard deviation which validated the repeatability of our manufacturing procedure for wearable graphene-based temperature sensor.

To ensure effective integration into wearable electronic applications, the mechanical flexibility and stability of the LRSNGO temperature sensor should be essentially evaluated. For this regard, a series of mechanical tests were performed on the LRSNGO sensor using a custom-built setup, see Fig. S2. Figure 8d gives the normalized sensor's resistance at different bending angles. The inset of Fig. 8d shows a photograph of the flexibility test at certain bending angles (*θ*). up to a 90° maximum bending angle, ~4.8% change of the LRSNGO sensor's resistance compared to its original flat value was recorded. The applied stress (*σ*) on the sensor was estimated at every point and recorded. Table S2 Summarizes all measurement calculations. The

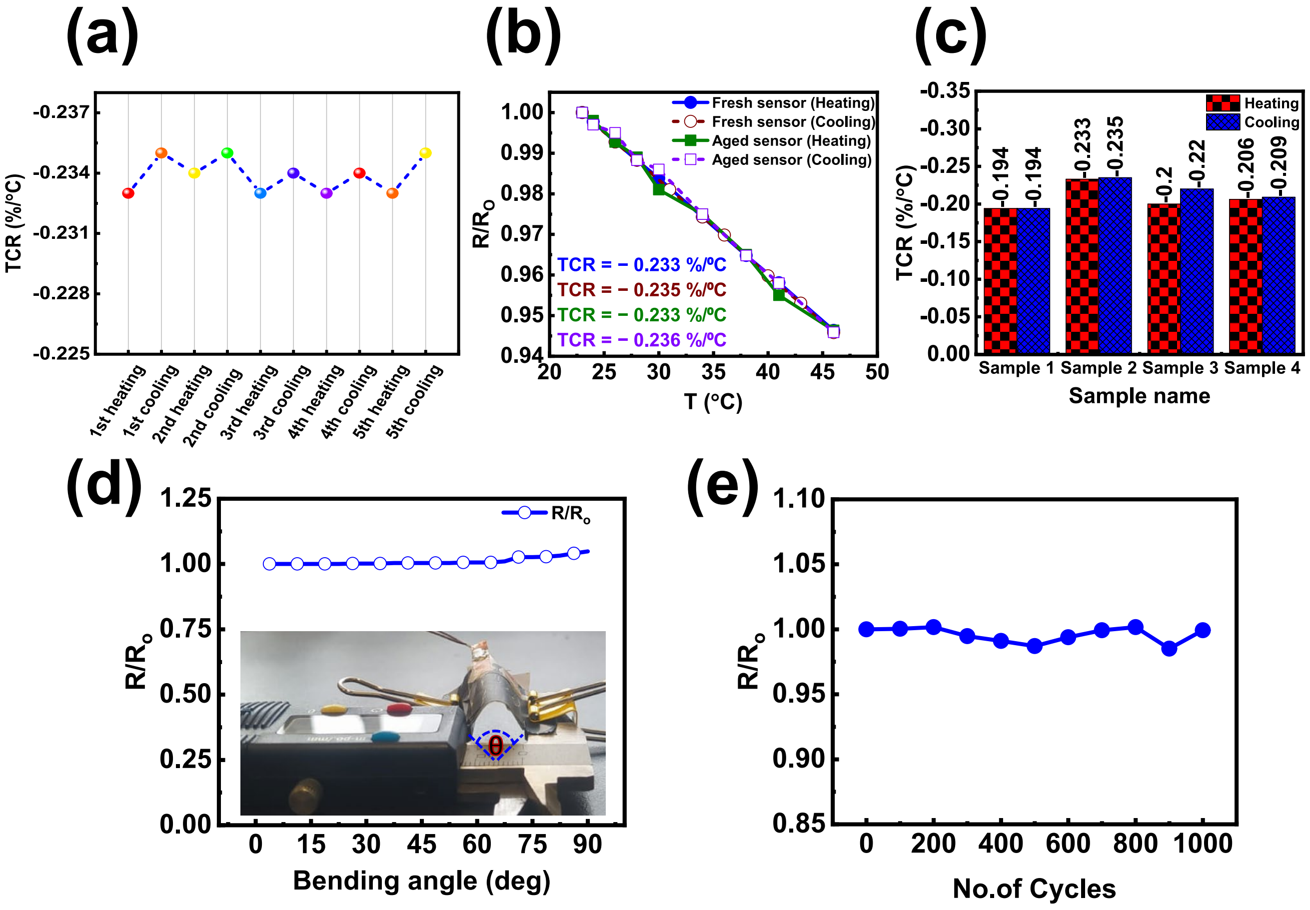

Fig. 8 Stability validation (**a**) LRSNGO thermal stability test results, (**b**) LRSNGO long-term stability test results, (**c**) LRSNGO sensors manufacturing repeatability results, temperature sensor flexibility (**d**) effect of bending angles on the sensor's resistance, and (**e**) effect of bending cycles on the sensor's resistance

maximum stress applied to the LRSNGO temperature sensor was 2.22 MPa at a bending angle of 90°, which implies the high integrity of the sensor. Also, the cyclic mechanical stability of the LRSNGO sensor was examined by Subjecting it to 500 bending cycles at an angle of 90º, and the sensor resistance was measured after each 100 bending cycles [80]. Figure 8e is a plot between the normalized sensor resistance versus the number of bending cycles. The plot shows that the LSNRGO sensor's resistance is almost unchanged at the end of the test, verifying its mechanical stability and high flexibility. This astonishing mechanical flexibility and stability is accredited to the ability of the overlapped graphene sheets to slip over each other during bending without losing electrical contact between each other. The high integrity and flexibility of the PET substrate also played a pivotal role in keeping the device pattern undeformed, maintaining coherence among graphene sheets during the test, and ensuring a delicate recovery at the end of the test. The overall results demonstrated that the LSNRGO sensor exhibited exceptional mechanical properties in addition to its excellent temperature sensing performance, which recommends it a strong candidate for practical wearable electronics applications.

3.4 Human temperature sensing application

To demonstrate the potential of the flexible LRSNGO temperature sensor as a wearable device for healthcare, electronic skins, human–machine interface, and other fields of application, the LRSNGO sensor was tested for Live monitoring of human body temperature. Firstly, the tested LRSNGO sensor was connected to a temperature logging circuit including an ADS 1115 analog to digital converter, an Arduino board, and a linear potentiometer as shown in Fig. 9a and Fig. S9 [81, 82]. The logging circuit was designed to utilize a voltage divider to monitor the sensor's resistance changes and a previously validated sensor measurements to compute and display the temperature. The Arduino was connected to MS Excel via data streamer to enable continuous temperature monitoring

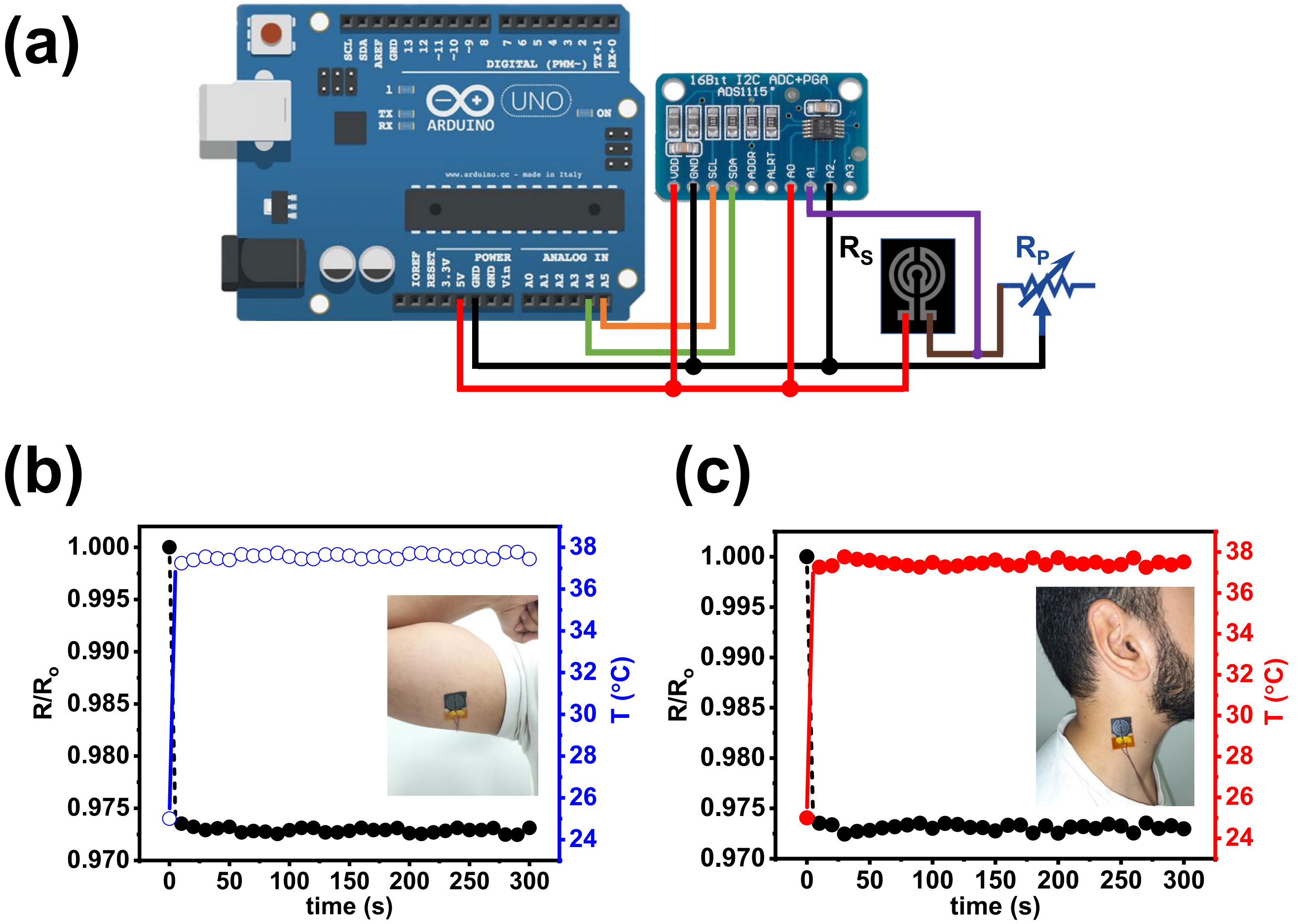

Fig. 9 Temperature sensor application (**a**) wiring diagram of the temperature logging circuit (**b**) temperature sensor response and fixation at temporal artery area (**c**) temperature sensor response and fixation at the neck area

every second. Then, the connected LRSNGO sensor was attached to a volunteer by means of thin double adhesive tape to guarantee good contact.

Among the several active spots on the human body for monitoring temperature, the tested sensor was stuck to the armpit area and the temporal artery area in the neck of a volunteer. These spots were carefully chosen to ensure accurate temperature measurements because of their proximity to blood flow. Figure 9b-c illustrates the live body temperature acquired by the LRSNGO sensor from the armpit and temporal artery areas, respectively. Both inset photos declare the comfortable attachment of the LRSNGO flexible sensor to the volunteer's body. By covering the sensor with thin tape serving as a shield to minimize heat transfer to the Surrounding air, temperature monitoring became more stable and the LRSNGO sensor demonstrated quick response and precision in both spots, with an almost consistent body temperature reading close to 37 °C, the typical human body temperature.

4 Conclusion

In summary, this work introduced a productive technique for fabricating flexible graphene-based temperature sensors using an affordable CNC diode laser writing tool. The precursors of the heteroatoms were directly mixed with GO aqueous solution using ultrasonication. Visible laser scribing was used for the concurrent photothermal reduction, heteroatom doping, and patterning of the GO thin films prepared on flexible PET substrates. XRD and Raman measurements showed that the sulfur and nitrogen co-doped laser-reduced graphene oxide (LRSNGO) has better structural and morphological characteristics than the nitrogen-doped and pristine LRGO in terms of higher crystallinity, lower defect density, and larger sp2 graphitic domains. SEM disclosed a similar surface morphology of all fabricated thin films but, the LRSNGO had a more compact thickness. XPS elemental analysis showed a successful integration of a higher dosage of nitrogen (3.0 at.%) and sulfur (1.3 at.%) Functionalities into the graphitic lattice of the LRSNGO causing enhanced free electrons donation and mitigated structural defects. As a result of the overall better characteristics, the LRSNGO temperature sensor demonstrated better electrical and thermal performances. A high electrical conductivity of 847.9 S/m and superior negative (TCR) of−0.233%/ºC was achieved by the LRSNGO temperature sensor, which is~94% and~117% higher than the LRNGO and pristine LRGO sensors, respectively. The astonishing temperature sensitivity of the LRNGO sensor was accompanied by performance Linearity, repeatability, durability, and high accuracy, in addition to a short response time of 3.5 s and a reasonable recovery time of~7.3 s. Finally, the mechanical flexibility and stability of the LRSNGO thin-film on PET substrate accentuated the high potential of heteroatom doping and visible diode laser-reduction as effective techniques for fabricating highly sensitive flexible temperature sensors to satisfy the desire in wearable electronics and the Internet of Things. LRSNGO sensor was tested for live monitoring of human body temperature demonstrated quick response and precision with an almost consistent body temperature reading.

Supplementary Information The online version contains supplementary material available at https://doi.org/10.1007/s42247-025-01226-1.

Acknowledgements The authors would like to express their sincere gratitude to Faculty of Engineering at Shoubra, Benha University, S. A. M. would like to acknowledge and thank Prof. Salah. S. A. Obayya and Mohamed Farahat from the Center for Photonic and Smart Materials (CPSM), Zewail city of science, technology, and innovation for their collaboration and support during the course of this project.

Authors' contribution statement **Amin Nabwy**: Methodology, Investigation, Conceptualization, Data curation, Writing original draft.
Mohammed Gamil: Writing — review & editing, Formal analysis, Conceptualization, Supervision.
Shaimaa A. Mohamed: Writing — review & editing, Methodology, Formal analysis, Data curation, Conceptualization.
Amr Hessein: Writing – review & editing, Methodology, Conceptualization, Formal analysis Supervision.

Funding Open access funding provided by The Science, Technology & Innovation Funding Authority (STDF) in cooperation with The Egyptian Knowledge Bank (EKB). The authors declare that no funds, grants, or other support were received during the preparation of this manuscript.

Data availability Data will be available on request.

Declarations

Competing interest The authors declare that they have no known competing financial interests or personal relationships that could have appeared to influence the work reported in this paper.

References

1. Q. Li, L.-N. Zhang, X.-M. Tao, X. Ding, Review of flexible temperature sensing networks for wearable physiological monitoring. Adv. Healthc. Mater. **6**, 1601371 (2017). https://doi.org/10.1002/adhm.201601371
2. G. Liu, Q. Tan, H. Kou, L. Zhang, J. Wang, W. Lv, H. Dong, J. Xiong, A flexible temperature sensor based on reduced graphene oxide for robot skin used in internet of things. Sensors (2018). https://doi.org/10.3390/s18051400
3. S. Wang, H. Zhai, Q. Zhang, X. Hu, Y. Li, X. Xiong, R. Ma, J. Wang, Y. Chang, L. Wu, Trends in flexible sensing technology in smart wearable mechanisms–materials–applications. Nanomaterials (2025). https://doi.org/10.3390/nano15040298
4. J. Shi, S. Liu, L. Zhang, B. Yang, L. Shu, Y. Yang, M. Ren, Y. Wang, J. Chen, W. Chen, Y. Chai, X. Tao, J. Shi, S. Liu, L. Zhang, B. Yang, W. Chen, Y. Chai, X. Tao, L. Shu, Y. Yang, M. Ren, Y. Wang, J. Chen, Smart textile-integrated microelectronic systems for wearable applications. Adv. Mater. (2019). https://doi.org/10.1002/adma.201901958
5. H.H. Asada, A. Reisner, Wearable sensors for human health monitoring, in: Smart Struct. Mater. Sensors Smart Struct. Technol. Civil, Mech. Aerosp. Syst. SPIE, 2006, 617401 (2006)
6. Y. Wang, Chapter 33 - Electronic skin, in: H.B.T.-N.-I.S. Haick (Ed.), Elsevier, 2025: pp. 487–504. https://doi.org/10.1016/B978-0-443-15684-7.00038-5
7. L. Liu, Y. Dou, J. Wang, Y. Zhao, W. Kong, C. Ma, D. He, H. Wang, H. Zhang, A. Chang, P. Zhao, Recent advances in flexible temperature sensors: materials, mechanism, fabrication, and applications. Adv. Sci. **11**, 2405003 (2024). https://doi.org/10.1002/advs.202405003
8. J. Li, Z. Fang, D. Wei, Y. Liu, Flexible pressure, humidity, and temperature sensors for human health monitoring. Adv. Healthc. Mater. **13**, 2401532 (2024). https://doi.org/10.1002/adhm.202401532
9. B. Zazoum, K.M. Batoo, M.A. Khan, Recent advances in flexible sensors and their applications. Sensors (2022). https://doi.org/10.3390/s22124653
10. S. Liu, Y. Rao, H. Jang, P. Tan, N. Lu, Strategies for body-conformable electronics. Matter **5**, 1104–1136 (2022). https://doi.org/10.1016/j.matt.2022.02.006
11. Y. Xu, Q. Fei, M. Page, G. Zhao, Y. Ling, D. Chen, Z. Yan, Laser-induced graphene for bioelectronics and soft actuators. Nano Res. **14**, 3033–3050 (2021). https://doi.org/10.1007/s12274-021-3441-9
12. B.A. Kuzubasoglu, S.K. Bahadir, Flexible temperature sensors: a review. Sensors Actuators A Phys. **315**, 112282 (2020). https://doi.org/10.1016/J.SNA.2020.112282
13. S. Yu, S. Wang, L. Zhao, S. Shi, L. Wang, H. Zheng, Ultra-flexible transparent temperature sensor with laser-direct writing of silver nanowire electrodes. Inorg. Chem. Commun. **170**, 113219 (2024). https://doi.org/10.1016/J.INOCHE.2024.113219
14. P. Sharma, S. Erfantalab, J. Dell, G. Parish, A. Keating, Micromachining porous silicon thin films for thermal sensing applications. Appl. Mater. Today **39**, 102320 (2024)
15. P. Sharma, S. Erfantalab, J. Dell, G. Parish, A. Keating, Using multilayer structures to enhance the electrical properties of porous silicon for thermal sensing. Appl. Mater. Today **35**, 102004 (2023)
16. J. Li, H. Nie, G. Zhou, Y. Hong, W. Meng, Y. Zhu, Q. Huang, High-resolution temperature sensor fabricated with composed PEDOT: PSS/CuPc for electronic skin. Sensors Actuators A Phys. **363**, 114706 (2023). https://doi.org/10.1016/j.sna.2023.114706
17. Y. Tian, J. Wang, H. Chen, H. Lin, S. Wu, Y. Zhang, M. Tian, J. Meng, W. Saeed, W. Liu, X. Chen, Electrospun multifunctional nanofibers for advanced wearable sensors. Talanta **283**, 127085 (2025). https://doi.org/10.1016/J.TALANTA.2024.127085
18. J. Sun, Z. Chen, L. Yuan, J. Xiang, W. Wang, Recent advances in flexible/stretchable sensors using laser-induced three-dimensional porous graphene: from precursor to manufacturing. Surf. Interfaces **55**, 105359 (2024). https://doi.org/10.1016/J.SURFIN.2024.105359
19. C. Tang, Y. Wang, Y. Li, S. Zeng, L. Kong, L. Li, J. Sun, M. Zhu, T. Deng, A review of graphene-based temperature sensors. Microelectron. Eng. **278**, 112015 (2023). https://doi.org/10.1016/J.MEE.2023.112015
20. Z. Chen, D. Zhao, R. Ma, X. Zhang, J. Rao, Y. Yin, X. Wang, F. Yi, Flexible temperature sensors based on carbon nanomaterials. J. Mater. Chem. B **9**, 1941–1964 (2021). https://doi.org/10.1039/D0TB02451A
21. S.S. Phadkule, S. Sarma, Progress in nanocomposite based flexible temperature sensors: a review. Meas. Sci. Technol. **27**, 100692 (2023). https://doi.org/10.1016/J.MEASEN.2023.100692
22. Y. Xue, J. Yang, P. Ye, B. Li, S. Gao, Y. Liu, J. Shi, J. Yang, L. Yuan, C. Guan, High-sensitivity fiber temperature sensor based on composite film structure and lossy mode resonance. Opt. Laser Technol. **181**, 111998 (2025). https://doi.org/10.1016/J.OPTLASTEC.2024.111998
23. P. Sehrawat, S.S. Abid, P. Islam, Mishra, Reduced graphene oxide based temperature sensor: Extraordinary performance governed by lattice dynamics assisted carrier transport. Sensors Actuators B Chem. **258**, 424–435 (2018). https://doi.org/10.1016/J.SNB.2017.11.112
24. K. Yang, C. Wu, G. Zhang, A state of review for graphene-based materials in preparation methods, characterization, and properties. Mater. Sci. Eng. B Solid-State Mater. Adv. Technol. **310**, 117698 (2024). https://doi.org/10.1016/J.MSEB.2024.117698
25. S. Yang, Y. Li, Y.-Y. Liang, W.-J. Wang, Y. Luo, J.-Z. Xu, Z.-M. Li, Graphene oxide induced isotactic polypropylene crystallization: role of structural reduction. RSC Adv. **6**, 23930–23941 (2016). https://doi.org/10.1039/c5ra26902d
26. B. Muchharla, T.N. Narayanan, K. Balakrishnan, P.M. Ajayan, S. Talapatra, Temperature dependent electrical transport of disordered reduced graphene oxide. 2D Mater. **1**, 11008 (2014). https://doi.org/10.1088/2053-1583/1/1/011008
27. K. Yokwana, B. Ntsendwana, E.N. Nxumalo, S.D. Mhlanga, Recent advances in nitrogen-doped graphene oxide nanomaterials: synthesis and applications in energy storage, sensor electrochemical applications and water treatment. J. Mater. Res. **38**, 3239–3263 (2023). https://doi.org/10.1557/s43578-023-01070-1
28. Y. Su, C. Ma, J. Chen, H. Wu, W. Luo, Y. Peng, Z. Luo, L. Li, Y. Tan, O.M. Omisore, Z. Zhu, L. Wang, H. Li, Printable, highly sensitive flexible temperature sensors for human body temperature monitoring: a review. Nanoscale Res. Lett. **15**, 200 (2020). https://doi.org/10.1186/s11671-020-03428-4
29. J. Liu, Y. Wang, X. Li, J. Wang, Y. Zhao, Graphene-based wearable temperature sensors: a review. Nanomaterials (2023). https://doi.org/10.3390/nano13162339
30. V. Naresh, U. Bhattacharjee, S.K. Martha, Boron doped graphene nanosheets as negative electrode additive for high-performance lead-acid batteries and ultracapacitors. J. Alloys Compd. **797**, 595–605 (2019). https://doi.org/10.1016/J.JALLCOM.2019.04.311
31. X.T. Gao, X.D. Zhu, L.L. Gu, C. Wang, K.N. Sun, Y.L. Hou, Efficient polysulfides anchoring for Li-S batteries: combined physical adsorption and chemical conversion in V2O5 hollow spheres wrapped in nitrogen-doped graphene network. Chem. Eng. J. **378**, 122189 (2019). https://doi.org/10.1016/J.CEJ.2019.122189
32. F.Y. Zheng, R. Li, S. Ge, W.R. Xu, Y. Zhang, Nitrogen and phosphorus co-doped carbon networks derived from shrimp shells as an efficient oxygen reduction catalyst for microbial fuel cells. J.

Power Sources **446**, 227356 (2020). https://doi.org/10.1016/J.JPOWSOUR.2019.227356
33. G. Zhao, D. Yu, H. Zhang, F. Sun, J. Li, L. Zhu, L. Sun, M. Yu, F. Besenbacher, Y. Sun, Sulphur-doped carbon nanosheets derived from biomass as high-performance anode materials for sodium-ion batteries. Nano Energy **67**, 104219 (2020). https://doi.org/10.1016/J.NANOEN.2019.104219
34. J.-J. Villora-Picó, G. Gil-Muñoz, A. Sepúlveda-Escribano, M.M. Pastor-Blas, The facile production of p-chloroaniline facilitated by an efficient and chemoselective metal-free N/S co-doped carbon catalyst. Int. J. Mol. Sci. (2024). https://doi.org/10.3390/ijms25179603
35. H. Lee, K. Paeng, I.S. Kim, A review of doping modulation in graphene. Synth. Met. **244**, 36–47 (2018). https://doi.org/10.1016/J.SYNTHMET.2018.07.001
36. F. Liu, Z. Wang, H. Zhang, L. Jin, X. Chu, B. Gu, H. Huang, W. Yang, Nitrogen, oxygen and sulfur co-doped hierarchical porous carbons toward high-performance supercapacitors by direct pyrolysis of kraft lignin. Carbon N. Y. **149**, 105–116 (2019). https://doi.org/10.1016/J.CARBON.2019.04.023
37. H. Wang, K. Zhang, Y. Song, J. Qiu, J. Wu, L. Yan, MnCo2S4 nanoparticles anchored to N- and S-codoped 3D graphene as a prominent electrode for asymmetric supercapacitors. Carbon N. Y. **146**, 420–429 (2019). https://doi.org/10.1016/J.CARBON.2019.02.035
38. T.S. Atabaev, S. Sayatova, A. Molkenova, I. Taniguchi, Nitrogen-doped carbon nanoparticles for potential temperature sensing applications. Sens. Bio-Sens. Res. **22**, 100253 (2019). https://doi.org/10.1016/j.sbsr.2018.100253
39. D.B. Gunjal, O.S. Nille, V.M. Naik, R. V Shejwal, G.B. Kolekar, A.H. Gore, Chapter 14 - Heteroatom/metal ion-doped carbon dots for sensing applications, in: S.K. Kailasa, C.M. Hussain (Eds.), Carbon Dots Anal. Chem., Elsevier, 2023: pp. 181–197. https://doi.org/10.1016/B978-0-323-98350-1.00002-5
40. J.A. Baimova, A. Santoro, G. Bella, N. Méndez-Lozano, F. Pérez-Reynoso, C. González-Gutiérrez, Eco-Friendly Approach for Graphene Oxide Synthesis by Modified Hummers Method (2022). https://doi.org/10.3390/ma15207228
41. J.L. Gómez-Delgado, J.J. Rodriguez-Molina, J.C. Perez-Angulo, N. Santos-Santos, E. Mejía-Ospino, Evaluation of the wettability alteration on sandstone rock by graphene oxide adsorption. Emergent Mater. **7**, 2045–2054 (2024). https://doi.org/10.1007/s42247-023-00596-8
42. M. Kassim Ali, A. Hessein, M.A. Hassan, M. Ghali, N.M. Shaalan, K. Nakamura, A. Abd El-Moneim, Corrigendum: Heteroatom-doped reduced graphene oxide/polyaniline nanocomposites with improved n-type thermoelectric performance. J Appl Polym Sci **139**, 51778 (2022). https://doi.org/10.1002/app.51778
43. N.S. Suhaimin, M.F.R. Hanifah, J. Jusin, J. Jaafar, M. Aziz, A.F. Ismail, M.H.D. Othman, M.A. Rahman, F. Aziz, N. Yusof, R. Mohamud, Tuning the oxygen functional groups in graphene oxide nanosheets by optimizing the oxidation time. Phys. E Low-Dimens. Syst. Nanostruct. **131**, 114727 (2021)
44. R.K. Sahoo, P. Gupta, P. Panda, A. Rath, B. Tripathy, P. Garg, S. Bedanta, U. Despande, S. Varma, Exploring superparamagnetic and intercalated Ag quantum particles in manganese oxide/graphene oxide for rapid and scalable organic pollutant removal. Emergent Mater. **7**, 1515–1530 (2024). https://doi.org/10.1007/s42247-024-00718-w
45. D. Lyu, S. Yao, Y. Bahari, S.W. Hasan, C. Pan, X. Zhang, F. Yu, Z.Q. Tian, P.K. Shen, In situ molecular-level synthesis of N, S co-doped carbon as efficient metal-free oxygen redox electrocatalysts for rechargeable Zn–Air batteries. Appl. Mater. Today **20**, 100737 (2020). https://doi.org/10.1016/j.apmt.2020.100737
46. Z. Wan, E.W. Streed, M. Lobino, S. Wang, R.T. Sang, I.S. Cole, D.V. Thiel, Q. Li, Laser-reduced graphene: synthesis, properties, and applications. Adv. Mater. Technol. **3**, 1700315 (2018). https://doi.org/10.1002/admt.201700315
47. L.J. Cote, J. Kim, Z. Zhang, C. Sun, J. Huang, Tunable assembly of graphene oxide surfactant sheets: wrinkles, overlaps and impacts on thin film properties. Soft Matter **6**, 6096–6101 (2010)
48. T. Wang, L.-X. Wang, D.-L. Wu, W. Xia, D.-Z. Jia, Interaction between nitrogen and sulfur in co-doped graphene and synergetic effect in supercapacitor. Sci. Rep. **5**, 9591 (2015). https://doi.org/10.1038/srep09591
49. S. Nathabumroong, C. Poochai, N. Chanlek, T. Eknapakul, S. Sonsupap, W. Tuichai, C. Sriprachuabwong, S. Rujirawat, P. Songsiririthigul, A. Tuantranont, R. Yimnirun, Enhanced surface and electrochemical properties of nitrogen-doped reduced graphene oxide by violet laser treatment for high charge storage and lower self-discharge supercapacitors. J. Power Sources **513**, 230517 (2021). https://doi.org/10.1016/J.JPOWSOUR.2021.230517
50. T. Katoh, G. Imamura, S. Obata, K. Saiki, Growth of N-doped graphene from nitrogen containing aromatic compounds: the effect of precursors on the doped site. RSC Adv. **6**, 13392–13398 (2016). https://doi.org/10.1039/C5RA22664C
51. S. Abdolhosseinzadeh, H. Asgharzadeh, H.S. Kim, Fast and fully-scalable synthesis of reduced graphene oxide. Sci. Rep. (2015). https://doi.org/10.1038/srep10160
52. S.H. Huh, X-ray diffraction of multi-layer graphenes: instant measurement and determination of the number of layers. Carbon N. Y. **78**, 617–621 (2014). https://doi.org/10.1016/j.carbon.2014.07.034
53. A.C. Ferrari, Raman spectroscopy of graphene and graphite: disorder, electron–phonon coupling, doping and nonadiabatic effects. Solid State Commun. **143**, 47–57 (2007). https://doi.org/10.1016/J.SSC.2007.03.052
54. A.C. Ferrari, D.M. Basko, Raman spectroscopy as a versatile tool for studying the properties of graphene. Nat. Nanotechnol. (2013). https://doi.org/10.1038/NNANO.2013.46
55. E.A. Ali, K. Elsaid, D.J. Hughes, M.M. Nasef, J.A. Syed, M. Ali, A. Abdel-Wahab, K. Ahmed, Z.K. Ghouri, N-doped and Se incorporated reduced graphene oxide nanocomposite as a new adsorbent for efficient Ni(II) ion removal from aqueous sample. Emergent Mater. **7**, 1031–1042 (2024). https://doi.org/10.1007/s42247-023-00608-7
56. A. Reina, X. Jia, J. Ho, D. Nezich, H. Son, V. Bulovic, M. Dresselhaus, J. Kong, Layer area, few-layer graphene films on arbitrary substrates by chemical vapor deposition. Nano Lett. **9**, 30–5 (2009). https://doi.org/10.1021/nl901829a
57. L.G. Cançado, A. Jorio, E.H.M. Ferreira, F. Stavale, C.A. Achete, R.B. Capaz, M.V.O. Moutinho, A. Lombardo, T.S. Kulmala, A.C. Ferrari, Quantifying defects in graphene via raman spectroscopy at different excitation energies. Nano Lett. **11**, 3190–3196 (2011). https://doi.org/10.1021/nl201432g
58. L. Li, J. Zhang, Z. Peng, Y. Li, C. Gao, Y. Ji, R. Ye, N. Dong. Kim, Q. Zhong, Y. Yang, H. Fei, G. Ruan, J.M. Tour, L. Li, J. Zhang, Z. Peng, Y. Li, C. Gao, Y. Ji, R. Ye, N.D. Kim, Q. Zhong, Y. Yang, H. Fei, G. Ruan, J.M. Tour, High-performance pseudocapacitive microsupercapacitors from laser-induced graphene. Adv. Mater. (2015). https://doi.org/10.1002/adma.201503333
59. A. Hamed, A. Hessein, A. Abd El-Moneim, Towards high performance flexible planar supercapacitors: in-situ laser scribing doping and reduction of graphene oxide films. Appl. Surf. Sci. **551**, 149457 (2021). https://doi.org/10.1016/J.APSUSC.2021.149457
60. G.K. Gupta, P. Sagar, M. Srivastava, A.K. Singh, S. Anwar, J. Singh, A. Kumar, S.K. Srivastava, A. Srivastava, Fabrication of manganese ferrite-reduced graphene oxide nanostructure as an electrode material for high performance supercapacitor. Emergent Mater. **7**, 1475–1487 (2024). https://doi.org/10.1007/s42247-024-00725-x

61. S. Bag, B. Mondal, A.K. Das, C.R. Raj, Nitrogen and sulfur dual-doped reduced graphene oxide: synergistic effect of dopants towards oxygen reduction reaction. Electrochim. Acta **163**, 16–23 (2015)
62. S. Uppugalla, R. Pothu, R. Boddula, M.A. Desai, N. Al-Qahtani, Nitrogen and sulfur co-doped activated carbon nanosheets for high-performance coin cell supercapacitor device with outstanding cycle stability. Emergent Mater. **6**, 1167–1176 (2023). https://doi.org/10.1007/s42247-023-00503-1
63. E. Biddinger, D. Deak, U. Ozkan, Nitrogen-containing carbon nanostructures as oxygen-reduction catalysts. Top. Catal. **52**, 1566–1574 (2009). https://doi.org/10.1007/s11244-009-9289-y
64. J.-H. Lee, H. Chen, E. Kim, H. Zhang, K. Wu, H. Zhang, X. Shen, Q. Zheng, J. Yang, S. Jeon, J.-K. Kim, Flexible temperature sensors made of aligned electrospun carbon nanofiber films with outstanding sensitivity and selectivity towards temperature †. Mater. Horiz. **8**, 1488 (2021). https://doi.org/10.1039/d1mh00018g
65. P.A. Denis, Band gap opening of monolayer and bilayer graphene doped with aluminium, silicon, phosphorus, and sulfur. Chem. Phys. Lett. **492**, 251–257 (2010). https://doi.org/10.1016/J.CPLETT.2010.04.038
66. A. DiFilippo, A. Chakraborty, M. Orlowski, Optimizing Electrical Conductivity of PEDOT:PSS Films: A Systematic Study of Individual and Combined Enhancement Techniques, (2024). https://doi.org/10.21203/rs.3.rs-4014120/v1
67. M.S. Abdel-Latif, M.H. El-Shafei, A. Hessein, A.A. El-Moneim, Flexible and freestanding temperature sensors based on laser carbonization of carbon nanofibers. Sens. Actuators, A **370**, 115280 (2024). https://doi.org/10.1016/J.SNA.2024.115280
68. S. Baek, J. Kim, P. Pujar, H.-J. Kwon, S. Kim, S. Gandla, Sub-zero temperature sensor based on laser-written carbon. Adv. Electron. Mater. (2022). https://doi.org/10.1002/aelm.202101252
69. R. Chen, T. Luo, D. Geng, Z. Shen, W. Zhou, Facile fabrication of a fast-response flexible temperature sensor via laser reduced graphene oxide for contactless human-machine interface. Carbon N. Y. **187**, 35–46 (2022). https://doi.org/10.1016/J.CARBON.2021.10.064
70. M. Singh, S. Kaushal, P. Singh, J. Sharma, Boron doped graphene oxide with enhanced photocatalytic activity for organic pollutants. J. Photochem. Photobiol. A, Chem. **364**, 130–139 (2018). https://doi.org/10.1016/j.jphotochem.2018.06.002
71. Z. Ramezani, H. Dehghani, Synthesis of strontium chromate-nitrogen and sulfur co-doped graphene and its potential for electrochemical hydrogen storage. Int. J. Hydrogen Energy **47**, 1026–1035 (2022). https://doi.org/10.1016/j.ijhydene.2021.10.057
72. L. Leontie, A. Carlescu, C. Doroftei, G. Rusu, V. Tiron, S. Gurlui, O. Susu, Electric and optical properties of some new functional lower-rim-substituted calixarene derivatives in thin films. Appl. Phys. A **124**, 355 (2018). https://doi.org/10.1007/s00339-018-1784-1
73. Y. Shin, Y.W. Kim, H.J. Kang, J.H. Lee, J.E. Byun, J.-Y. Yang, J.W. Lee, Stretchable and skin-mountable temperature sensor array using reduction-controlled graphene oxide for dermatological thermography. Nano Lett. **23**, 5391–5398 (2023). https://doi.org/10.1021/acs.nanolett.2c04752
74. H. Cho, C. Lee, C. Lee, S. Lee, S. Kim, Robust, ultrathin, and highly sensitive reduced graphene oxide/silk fibroin wearable sensors responded to temperature and humidity for physiological detection. Biomacromolecules **24**, 2606–2617 (2023). https://doi.org/10.1021/acs.biomac.3c00106
75. J. Štulík, O. Musil, F. Josefík, P. Kadlec, Graphene-based temperature sensors-comparison of the temperature and humidity dependences. Nanomaterials (2022). https://doi.org/10.3390/nano12091594
76. S. Gandla, M. Naqi, M. Lee, J. Joon. Lee, Y. Won, P. Pujar, J. Kim, S. Lee, S. Kim, S. Gandla, M. Naqi, J.J. Lee, Y. Won, P. Pujar, S. Kim, M. Lee, J. Kim, S. Lee, Highly linear and stable flexible temperature sensors based on laser-induced carbonization of polyimide substrates for personal mobile monitoring. Adv. Mater. Technol., 2000014 (2020). https://doi.org/10.1002/admt.202000014
77. X. Li, D. Su, Y. Gu, J. Zhang, S. Li, Y. Xiao, J. He, W. Wang, D. Li, Laser fabrication of epidermal paper-based graphene sensors. Appl. Mater. Today **36**, 102051 (2024). https://doi.org/10.1016/j.apmt.2023.102051
78. Y. Zhang, C. Zhao, C. Yu, Y. Li, X. Guo, Y. Zhang, C. Chen, L. Cao, High-linearity graphene-based temperature sensor fabricated by laser writing. J. Mater. Sci. Mater. Electron. **35**, 109 (2024). https://doi.org/10.1007/s10854-023-11841-5
79. S. Burt, M. Podesta, Response times of meteorological air temperature sensors. Q. J. R. Meteorol. Soc. (2020). https://doi.org/10.1002/qj.3817
80. K. Fu, R.-Q. Xu, J. Chen, Effect of bending stress on the conductive properties of two-dimensional graphene, Yingyong Kexue Xuebao/Journal. Appl. Sci. **34**, 163–170 (2016). https://doi.org/10.3969/j.issn.0255-8297.2016.02.006
81. C.S. Buga, J. Viana, A design of experiments study on inkjet printed PEDOT:PSS temperature sensors. IEEE Sens. J. (2024). https://doi.org/10.1109/JSEN.2024.3363870
82. C.S. Buga, J. Viana, Development and characterization of flexible carbon temperature sensors: a study on different inks and sensor designs. Sens. Actuators, A **378**, 115823 (2024). https://doi.org/10.1016/j.sna.2024.115823